Linear model of water movements for large-scale inverted siphon in water distribution system

Mao Zhonghao, Guan Guanghua, Yang Zhonghua and Zhong Ke

ABSTRACT

This paper proposes a linear model that relates the pressure head variations at the downstream end of an inverted siphon to the flow rate variations at two ends. It divides the pressure head variations in the inverted siphon into low-frequency part and high-frequency part. The two parts are caused by the deformation of the siphon wall and the reflection of acoustic wave, respectively. In order to build a simplified relation between wall deformation and low-frequency pressure head variations, the Preissmann slot method (PSM) is adopted in this paper. The linear model can also be used in other forms of structures, such as pipes and tunnels, where a pressurized flow condition is present. In comparison with simulation results using the finite volume method, the linear model shows an L_2 norm of 0.177 for a large-scale inverted siphon and 0.044 for a PVC pipe. To this end, the linear model is adopted to model a large-scale inverted siphon in a virtual water delivery system. Simulation results show that the inverted siphon can reduce water fluctuations. An equation to quantify this effect is proposed based on the linear model.

Key words | canal automatic control, frequency domain analysis, large-scale inverted siphon, linear model, pressurized flow, PVC pipe

Mao Zhonghao
Guan Guanghua (corresponding author)
Yang Zhonghua
Zhong Ke
State Key Laboratory of Water Resources and Hydropower Engineering Science,
Wuhan University,
430072 Wuhan,
China
E-mail: *ggh@whu.edu.cn*

NOTATION

A_f	wetted area of full cross-section in m^2
a	speed of acoustic wave in m/s
B_{sl}	width of Pressimann slot in m
h	relative water elevation in m
h_f	frictional head loss of quasi-steady flow in m
h_i	inertia head in m
$Imag$	resonance frequency in rad/s
q	relative discharge in m^3/s
s	Laplace variable in s^{-1}
y	water depth in m
τ	delay time of propagation downstream in s

INTRODUCTION

Under the present changing climate, the conflict between water demand and water supply has become more and more critical. In order to balance the water resources in western and eastern areas of China, some long distance water distribution systems are being built. However, a large amount of water is wasted due to the low management level in these systems. Canal automatic control is an efficient tool to maintain stable flows, improve water-use efficiency and fulfill users' demands in a timely manner. It is achieved by automatic operations of control structures based on periodical observations of canal systems (Malaterre *et al.* 1998; Clemmens *et al.* 2005; Clemmens & Strand 2010). Commonly, a water level monitor is fixed at a certain point in an open-channel; this point is referred to as the target point. The water level at the target point is sent to a feedback controller periodically and a control algorithm is adopted to decide the opening of check gates so that the water surface at the target point can keep a designed level. For example, when the water surface at the target point is

doi: 10.2166/hydro.2019.053

lower than the designed level, the check gate upstream is raised and more water is let into the open-channel so that the water surface goes up, while the feedback controller determines the movement of check gates according to the water level at the target point. A sketch to illustrate this system is shown in Figure 1.

After the check gate is raised, there is a delay time before the water level at the target point starts to rise due to the wave movement in the open-channel. Therefore, the feedback controller needs to predict the water level variations at the target point corresponding to the movement of the check gate (Clemmens *et al.* 2015; Wahlin & Zimbelman 2018). Water in open-channels can be simulated using the Saint-Venant (S-V) equations (Cunge *et al.* 1980; Rogers *et al.* 1993). However, when it comes to the design of feedback controller, the S-V equations are not easily implementable due to the large number of parameters involved. Based on the understanding of wave movements in open-channels, researchers have proposed a linear model as a simplification of the S-V equations (Schuurmans *et al.* 1999). Schuurmans's model contains a delay section that represents the delay time of wave movement in the open-channel and an integer section that reflects the effect of water volume in the open-channel on the water level at the target point; therefore, this model is referred to as the ID (integer-delay) model. The parameters of the ID model can be derived using the size of open-channels or field data, the latter of which makes it more robust (Foo *et al.* 2012, 2014). Furthermore, the ID model can be used in optimization of the feedback controller due to its simplicity (Overloop *et al.* 2005). Litrico & Fromion (2004) improved the accuracy of the ID model by adding two new parameters, which became the integer-delay-zero (IDZ) model.

In previous studies, canal automatic control is limited to open-channels because only linear models for open-channels have been proposed (Guan *et al.* 2011; Shahdany *et al.* 2016). Pressure distribution in an inverted siphon or pipe is influenced by the boundary conditions, the flow rate distribution, and the material of the siphon (or pipe) wall (Sadeghi *et al.* 2012; Okhravi *et al.* 2017). The wave movements in an inverted siphon are very different from that in free-surface flows. The speed of acoustic wave can reach 1,000 m/s which is two orders of magnitude higher than the wave speed in open-channels, indicating that the delay time between check gate movement and water level variations at the target point is much smaller (Brito *et al.* 2017; Li *et al.* 2018). Moreover, unlike in the open-channel where wave dissipates quickly due to wall friction and gravity, the wave in an inverted siphon may reflect for many times before it is completely damped. In addition, the influence of the wall deformation on pressure head variations must be taken into consideration (Zhu *et al.* 2018).

In order to apply canal automatic control to complex water distribution systems consisting of a large-scale inverted siphon, a new linear model that is especially tailored to describe the wave movements in an inverted siphon is required for the design of feedback controller. Due to the high speed of acoustic wave, the pressure head

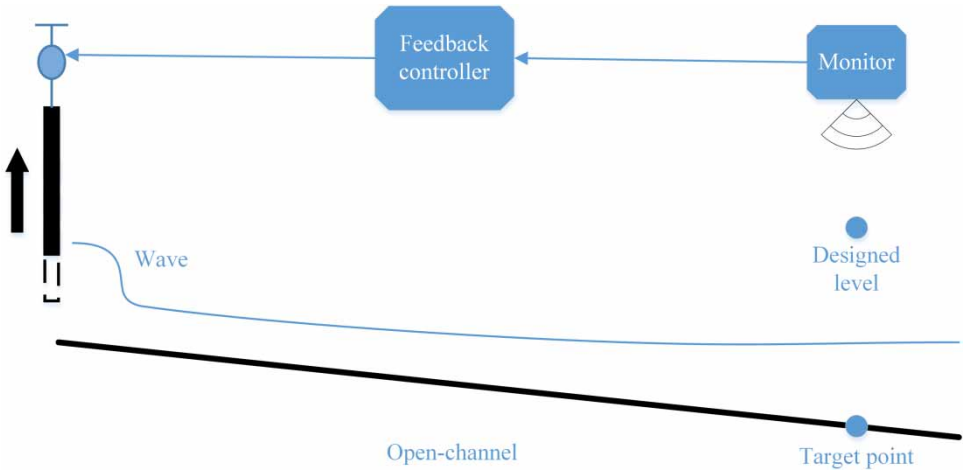

Figure 1 | A sketch of the automatic control system in an open-channel.

variations are very frequent and hard to analyze in the time domain. Frequency analysis has been shown as an efficient tool for evaluating the relation between pressure head variations and flow rate variations. It has been widely used in leakage detection in pressurized pipelines (Duan *et al.* 2011; Wang & Ghidaoui 2018; Lin *et al.* 2019). In this paper, frequency analysis is used to evaluate pressure head variations at the downstream end of an inverted siphon using the flow rate at two ends. The Preissmann slot method (PSM) is used in this paper to build a simplified relation between wall deformation and pressure head variations for the first time. The linear model proposed in this paper can be used for other forms of structures, like pipes and tunnels, where a pressurized flow condition is present. It can be used to construct a coupled linear model of open-channels and inverted siphons, which can then optimize controller design and improve the management level of complex water distribution systems.

This paper consists of five sections. The first section introduces the ID model and the IDZ model, as well as the PSM. The following section investigates characteristics of pressurized flows in inverted siphon using frequency analysis. The linear model is proposed and validated in the next section, then a section describes the linear model being used to model an inverted siphon in a virtual water distribution system. Conclusions are drawn in the final section.

Preissmann slot method

The PSM has been widely used in modelling transitions between free-surface flow and pressurized flow (Dazzi *et al.* 2016; An *et al.* 2018; Maranzoni & Mignosa 2018). It permits simulation of two flow regimes using one set of governing equations, i.e., the S-V equations, by assuming a narrow slot on the top of pressurized flow and forming a virtual free-surface flow, shown in Figure 2.

The water height inside the slot represents the pressure head above the top of the cross-section. To guarantee that the gravity wave speed inside the slot equals the acoustic wave speed in pressurized flow, the width of slot B_{sl} is computed as:

$$B_{sl} = \frac{gA_f}{a^2} \tag{1}$$

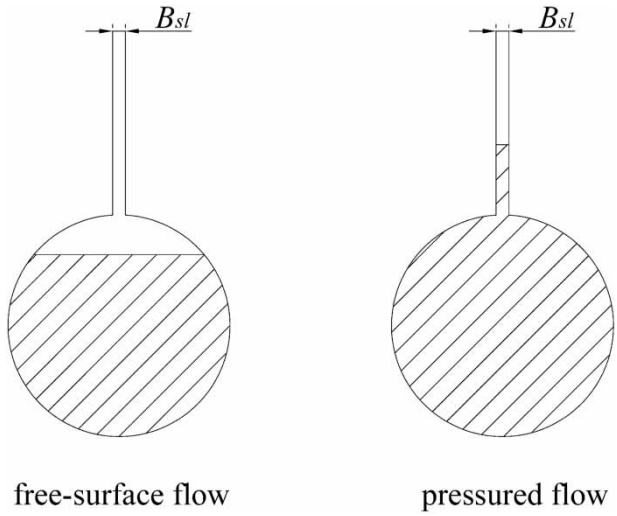

Figure 2 | The Preissmann slot method.

where A_f is the wetted area of the full cross-section; a is the speed of acoustic wave which can be computed according to the Korteweg-Joukowsky formula:

$$a = \frac{\sqrt{\frac{K}{\rho}}}{\sqrt{1 + \frac{KD}{Eb}}} \tag{2}$$

where ρ is the density of the liquid; K is the bulk modulus of elasticity of the liquid; E is the modulus of elasticity of wall material; b is the thickness of wall. With the PSM, the pressurized flow can be simulated using the modified S-V equations:

$$\frac{\partial H}{\partial t} + v\frac{\partial H}{\partial x} + \frac{A}{B_{sl}}\frac{\partial v}{\partial x} = 0 \tag{3}$$

$$g\frac{\partial H}{\partial x} + v\frac{\partial v}{\partial x} + \frac{\partial v}{\partial t} = g(S_0 - S_f) \tag{4}$$

where H is pressure head; v is flow velocity; A is wetted area; g is acceleration of gravity; $S_f = n^2v^2/R^{4/3}$ is hydraulic slope; n is Manning coefficient; R is hydraulic radius; S_b is bed slope.

The purpose of using PSM to model pressurized flow in an inverted siphon is to build a simple relation between wall deformation and pressure head variation. For an inverted siphon with a circular cross-section, according to the elasticity of siphon wall, the relation between wetted area

A and pressure head H follows:

$$\frac{dA}{dH} = \frac{AD\rho g}{Eb} \tag{5}$$

Neglecting the '1' in the denominator of Equation (2) and insert it into Equation (1):

$$B_{sl} = \frac{AD\rho g}{Eb} \tag{6}$$

According to Equations (5) and (6):

$$\frac{dA}{dH} = B_{sl} \tag{7}$$

As shown by Equation (7), the width of the virtual slot B_{sl} can be regarded as the ratio of wall deformation to pressure head variations, it is a parameter which reflects the wall material, wall size, and wave speed. Equation (7) is a simplified relation because it ignores the time-dependent nature of stress-strain behavior of the wall material (Bertaglia *et al.* 2018). In this paper, it is used to derive the linear model of inverted siphon for its simplicity.

ID model and IDZ model of open-channel

The ID model and IDZ model are derived from the linearized S-V equations around a steady state defined by $Q_0(x)$ and $Y_0(x)$, where Q is flow rate and Y is water depth. Assume $Q(x, t) = Q_0(x) + q(x, t)$, and $Y(x, t) = Y_0(x) + y(x, t)$:

$$B_0\frac{\partial y}{\partial t} + \frac{\partial q}{\partial x} = 0 \tag{8}$$

$$\begin{aligned}&\frac{\partial q}{\partial t} + 2v_0\frac{\partial q}{\partial x} + (c_0^2 - v_0^2)B_0(x)\frac{\partial y}{\partial x} + \left[\frac{2g}{v_0}\left(S_{f0} - \frac{v_0^2 B_0}{gA_0}\frac{dY_0}{dx}\right)\right]q \\ &- \left\{v_0^2\frac{dB_0}{dx} + gB_0\left[\left(\frac{7}{3} - \frac{4A_0}{3T_0P_0}\frac{\partial P_0}{\partial Y}\right)S_{f0} \right.\right. \\ &\left.\left. + S_b - \left(1 + 2\frac{v_0^2 B_0}{gA_0}\right)\frac{dY_0}{dx}\right]\right\}y = 0\end{aligned} \tag{9}$$

where v_0, c_0, B_0, S_{f0}, Y_0, A_0, T_0, and P_0 (wetted perimeter) are functions of x; c_0 is the speed of gravity wave; and 0 denotes the value of each term at the initial state (Schuurmans *et al.* 1995). In the ID model, an open-channel is divided into uniform flow area and backwater area. The flow profile is parallel to the bed in uniform flow area and almost horizontal in the backwater area, as shown in Figure 3.

In Figure 3, $q_1 = Q(0, t) - Q_0(0)$, $y_1 = Y(0, t) - Y_0(0)$, $q_2 = Q(L, t) - Q_0(L)$, $y_2 = Y(L, t) - Y_0(L)$ and L is the length of open-channel. Schuurmans proved that the wave traveling upstream dampens exponentially with distance whereas the wave moving downstream always reaches the downstream end in open-channels. The variations of water depth in the backwater area can be computed using the water volume variations in the backwater area:

$$\frac{d}{dt}y_2(t) = \frac{1}{A_s}[q_1(t - \tau)q_2(t)] \tag{10}$$

where A_s is the surface area of backwater; τ is the travelling time of wave from upstream end to downstream end (Schuurmans *et al.* 1995, 1999). Litrico & Fromion (2004) proposed to add two new parameters to improve the accuracy of the ID model:

$$\begin{aligned}&\frac{d}{dt}y(t) = \frac{1}{A_s}[q_1(t - \tau) - q_2(t)] \\ &y_2(t) = y(t) + b_u q_1(t - \tau) - b_d q_2(t)\end{aligned} \tag{11}$$

where $y(t)$ is an intermediate variable; b_u and b_d are parameters that reflect the instantaneous variations of y_2 when wave peak is present at the downstream end. Figure 4 is a sketch of h_2 computed using the ID model, the IDZ model, and the realistic variations. Before $t = t_0$, a steady flow condition is ensured, then a step change q_1 at the

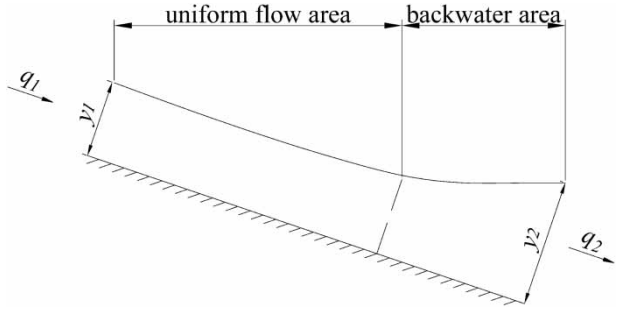

Figure 3 | Uniform flow area and backwater area of open-channel.

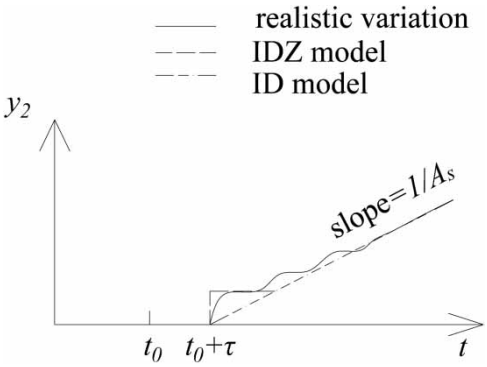

Figure 4 | A sketch of y_2 computed using ID model, IDZ model, and the realistic variation.

upstream end arises. During the time the wave is travelling to the downstream end, y_2 equals zero. As soon as it reaches the backwater area, the water depth at the downstream end rises. In spite of the wave peak, the rising speed of y_2 equals q_1/A_s, as shown in Figure 4.

The ID model and the IDZ model are not appropriate for inverted siphons due to the different flow characteristics. In this paper, the authors propose a linear model that describes the variations of pressure head in inverted siphon as a combination of a low-frequency part and high-frequency part.

FREQUENCY DOMAIN ANALYSIS

In water delivery systems, most inverted siphons consist of a single closed conduit or several parallel closed conduits with circular cross-sections. In this paper, the linearized S-V equations which are modified by the PSM for a prismatic inverted siphon with a circular cross-section are derived:

$$B_{sl}\frac{\partial h(x,t)}{\partial t}+\frac{\partial q(x,t)}{\partial x}=0 \tag{12}$$

$$\frac{\partial q}{\partial t}+2v_0\frac{\partial q}{\partial x}+(a_0^2-v_0^2)B_{sl}\frac{\partial h}{\partial x}+\frac{2g}{V_0}S_{f0}q-\left[g\left(\frac{5}{3}S_{f0}+S_b\right)\right]B_{sl}h=0 \tag{13}$$

where H is pressure head and $H(x,\ t)=H_0(x)+h(x,\ t)$, $h_1=H(0,\ t)-H_0(0)$ and $h_2=H(L,\ t)-H_0(L)$; L is length of inverted siphon. The derivation of Equations (12) and (13) is listed in the Appendix. The state-transition matrix can be obtained by applying a Laplace transform to Equations (12) and (13):

$$\begin{bmatrix} B_{sl}\bullet q_2(s) \\ h_2(s)\end{bmatrix}=\boldsymbol{\Phi}(L,s)\begin{bmatrix} B_{sl}\bullet q_1(s) \\ h_1(s)\end{bmatrix} \tag{14}$$

where $q_1(s)$ and $q_2(s)$ are the Laplace transforms of $q_1(t)$ and $q_2(t)$, $h_1(s)$ and $h_2(s)$ are Laplace transforms of $h_1(t)$ and $h_2(t)$, respectively. $\boldsymbol{\Phi}(L,\ s)$ is state-transition matrix of $q_1(s)$, $h_1(s)$ and $q_2(s)$, $h_2(s)$; for the derivation of $\boldsymbol{\Phi}(L,\ s)$, readers are referred to Litrico & Fromion (2004). The transfer function between $h_2(s)$ and $q_1(s)$ is noted as p_{21}. The transfer function between $h_2(s)$ and $q_2(s)$ is noted as p_{22}.

$$p_{21}=\frac{(\lambda_2(s)-\lambda_1(s))e^{(\lambda_1(s)+\lambda_2(s))L}}{(e^{\lambda_2(s)L}-e^{\lambda_1(s)L})B_{sl}s} \tag{15}$$

$$p_{22}=\frac{(\lambda_1(s)e^{\lambda_1(s)L}-\lambda_2(s))e^{\lambda_2(s)L}}{(e^{\lambda_2(s)L}-e^{\lambda_1(s)L})B_{sl}s} \tag{16}$$

where $\lambda_1(s)$ and $\lambda_2(s)$ are eigenvalues of $\boldsymbol{\Phi}(L,\ s)$.

In this paper, two scenarios are investigated. Scenario A is an inverted siphon in the Dianzhong water distribution system. It consists of five parallel closed conduits and each one has a circular cross-section, shown as Figure 5. The parameters of scenario A are listed in Table 1. The speed of acoustic wave is 1,014 m/s according to the Korteweg-Joukowsky formula. The slot width is computed using Equation (1) and is 5.9885×10^{-4} m.

Scenario B is an experimental horizontal polyvinyl chloride (PVC) pipe, shown as Figure 6. In order to avoid the vibration of PVC pipe, it is fixed to a concrete foundation. Its parameters are listed in Table 2. The speed of acoustic wave which is validated by experiments is 348 m/s, and the slot width computed using Equation (1) is 3.5218×10^{-6} m.

Bode plots of transfer function

Bode plot is a common method to study transfer functions in frequency domain. Its abscissa is frequency (Freq rad/s) of input and its ordinate is magnification (Gain dB) and phase difference (Phase degree) of output. Figures 7–10

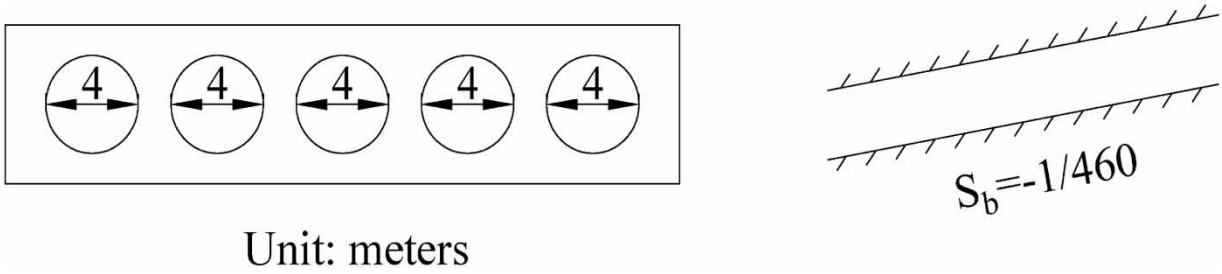

Figure 5 | Longitudinal sketch and cross-section of scenario A.

Table 1 | Parameters of scenario A

Diameter (m)	4
Number of conduits	5
Length (m)	516
Acoustic wave speed (m/s)	1,014
Designed flow rate (m^3/s)	120
Bed slope	−1/460
Manning coefficient	0.014
Slot width (m)	5.9885×10^{-4}

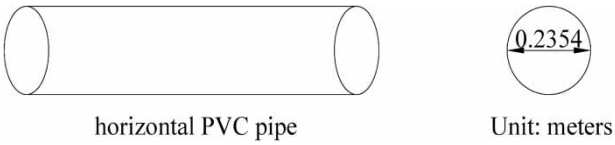

Figure 6 | Longitudinal sketch and cross-section of PVC pipe.

Table 2 | Parameters of scenario B

Diameter (m)	0.2354
Length (m)	271.3
Acoustic wave speed (m/s)	348
Designed flow rate (m^3/s)	0.007
Bed slope	0
Manning coefficient	0.010
Slot width (m)	3.5218×10^{-6}

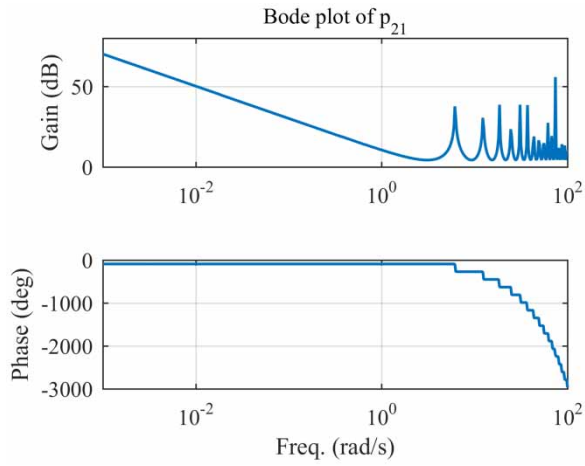

Figure 7 | Bode plot of p_{21} of scenario A.

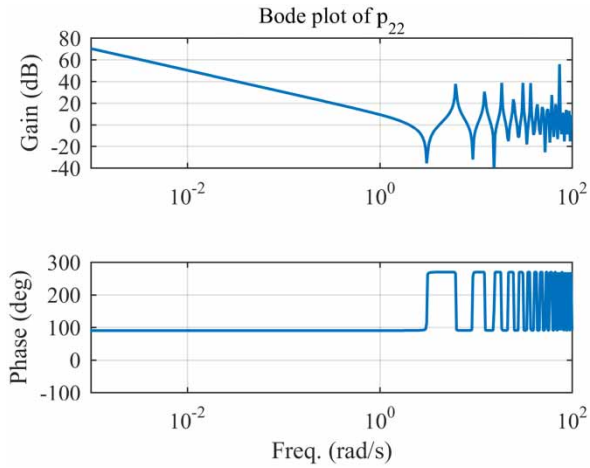

Figure 8 | Bode plot of p_{22} of scenario A.

are bode plots of p_{21} and p_{22} which contain 500 frequency points that range from 0.001 rad/s to 100 rad/s.

At low-frequency domain where $Freq < 1$ rad/s, the magnification line of p_{21} is straight with a slope of −20 dB while the phase line is horizontal. Thses lines are the same as that of an integrator section. The phase line is below zero in low-frequency domain, which means there is a delay in p_{21}. Thus p_{21} can be estimated by an integrator section and a delay section. The magnification line of p_{22} is similar to that of p_{21} at low-frequency domain. However, the phase line is above zero indicating that there is no

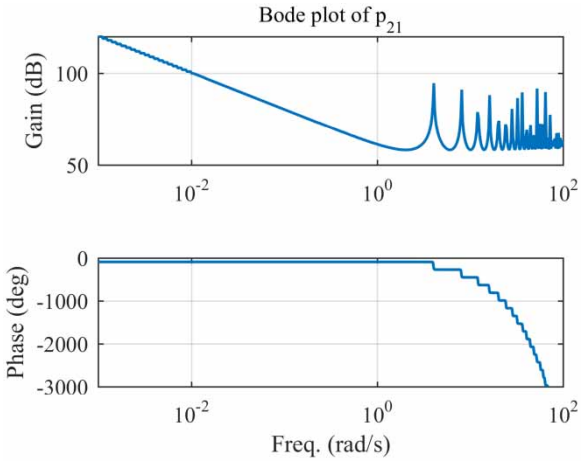

Figure 9 | Bode plot of p_{21} of scenario B.

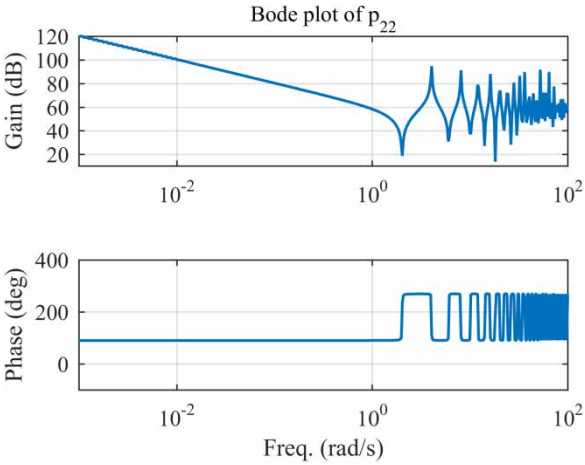

Figure 10 | Bode plot of p_{22} of scenario B.

delay time in p_{22}. Thus, p_{22} can be estimated by an integrator section only. For $Freq > 1$ rad/s, the magnification lines of p_{21} and p_{22} change in an oscillatory manner indicating that waves are superimposed in high-frequency domain. Several frequencies of the magnification peaks are studied in the following text.

Poles of transfer function

Normally, frequencies that are close to the poles of transfer function have larger magnification. According to Equations (15) and (16), the poles of p_{21} and p_{22} are given by:

$$(e^{\lambda_2(s)L} - e^{\lambda_1(s)L})B_{sl}S = 0 \tag{17}$$

The imaginary part of the No. k pole can be calculated by solving Equation (17) which is:

$$Imag = \frac{2\alpha^2\beta^2}{(\alpha+\beta)^2}\sqrt{\Delta(k)},\ \ k = 0, 1, 2\ldots,$$
$$\Delta(k) = \frac{(\alpha+\beta)^2}{\alpha^2\beta^2}\left[\frac{(\alpha\delta-\gamma)(\beta\delta-\gamma)}{\alpha\beta(\alpha+\beta)^2} - \frac{k^2\pi^2}{L^2}\right] \tag{18}$$

The expressions of α, β, σ, and γ are as follows:

$$\alpha = a_0 + v_0,$$
$$\beta = a_0 - v_0,$$
$$\sigma = \frac{2g}{v_0}S_{f0}, \tag{19}$$
$$\gamma = g\left(\frac{8}{3}S_{f0} + 2S_b\right)$$

In order to get a simplified expression of *Imag*, the authors assume σ and γ to be zero, which is a frictionless and horizontal case. Under this assumption, Equation (18) becomes:

$$Imag = \frac{2k\pi}{\left(\frac{L}{\alpha}+\frac{L}{\beta}\right)} \tag{20}$$

Imag of the first five poles and frequencies of the first five magnification peaks in two scenarios are listed in Table 3. Where k is the serial number of pole, $j^2 = -1$. It is shown that the frequencies are close to the imaginary part of poles with a difference of less than 0.2 rad/s which is introduced due to the selected finite frequencies.

Table 3 | *Imag* of poles and frequencies of peaks of scenario A and B

K	*Imag* of scenario A (j)	Frequencies of magnification peaks of scenario A (rad/s)	*Imag* of scenario B (j)	Frequencies of magnification peaks of scenario B (rad/s)
0	0		0	
1	6.1736	6.132	4.0298	4.048
2	12.3471	12.25	8.0595	8.088
3	18.5207	18.56	12.0893	11.97
4	24.6943	24.48	16.1190	16.16
…	…	…	…	…

Note that $L/\alpha + L/\beta$ is the duration time of a wave moving in an inverted siphon back and forth once. It can be derived that for q_1 and q_2, whose frequencies are multiples of wave reflection, frequency causes larger amplitude of h_2 as a resonance. To validate this conclusion, a series frequencies of q_1 around 6.132 rad/s are simulated for scenario A, and a series frequencies of q_1 around 4.048 rad/s are simulated for scenario B. The simulated frequencies are shown in Figures 11 and 12. The amplitudes of q_1 for scenario A and scenario B are 0.01 and 0.001 m^3/s, respectively. The results are shown in Figures 13 and 14.

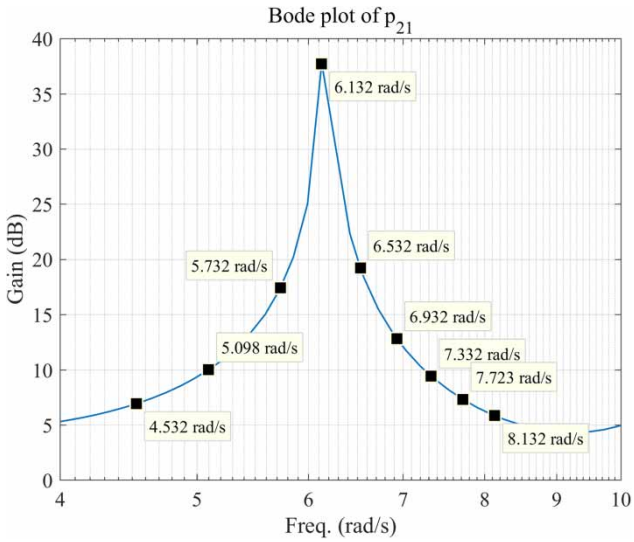

Figure 11 | Frequency points for simulation of scenario A.

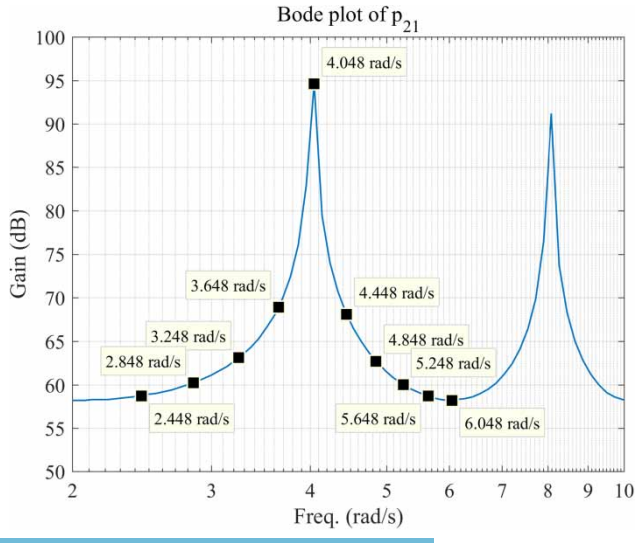

Figure 12 | Frequency points for simulation of scenario B.

For scenario A, q_1 with a frequency of 6.132 rad/s (solid line) causes the largest amplitude in variations of h_2 among all the tested frequencies. This conclusion can also be applied to scenario B. In order to avoid the large amplitude of pressure head variations in inverted siphons and pipes, flow rate change whose frequencies are close to the frequencies computed using Equation (20) should be avoided.

LINEAR MODEL OF INVERTED SIPHON

According to Equation (7), the ratio of wall deformation to pressure head variation equals the virtual slot width B_{sl}. Considering that wall deformation is a gradual process, the deformation at the outlet can be approximated using the average deformation along the siphon and pipe. Neglecting the compressibility of water, the average wall deformation can be quantified using the variations of water volume in the siphon:

$$dA = \frac{dV}{L} \tag{21}$$

where V is the total volume of water in the siphon or pipe. In addition, the variations of water volume can be computed using the flow rate at inlet and outlet:

$$\frac{dV}{dt} = (q_1(t-\tau) - q_2(t)) \tag{22}$$

where τ is the delay time of acoustic wave that travels to downstream end from upstream end, it can be computed approximately using:

$$\tau = \frac{L}{a} \tag{23}$$

Applying Equations (23) and (21) to Equation (22), the low-frequency variations of pressure head can be computed using:

$$\frac{dh_{2low}(t)}{dt} = \frac{1}{B_{sl} \bullet L}\left(q_1\left(t - \frac{L}{a}\right) - q_2(t)\right) \tag{24}$$

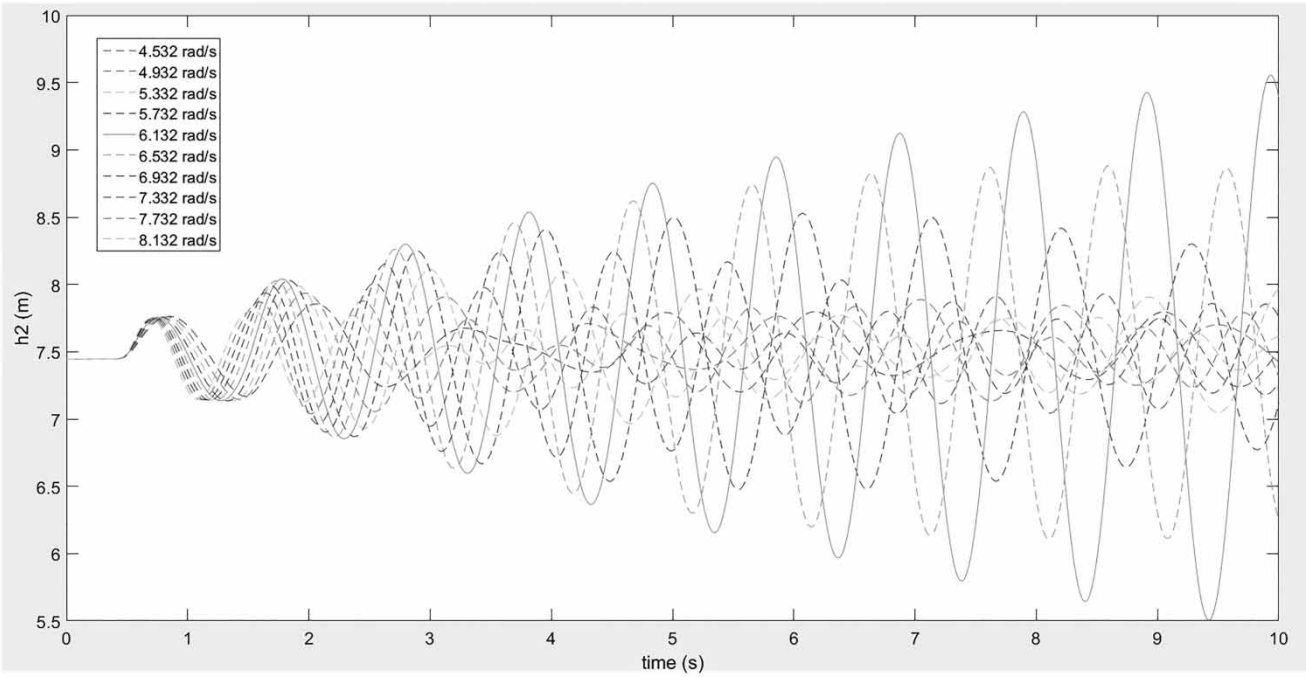

Figure 13 | Plots of h_2 of scenario A for different frequencies of q_1.

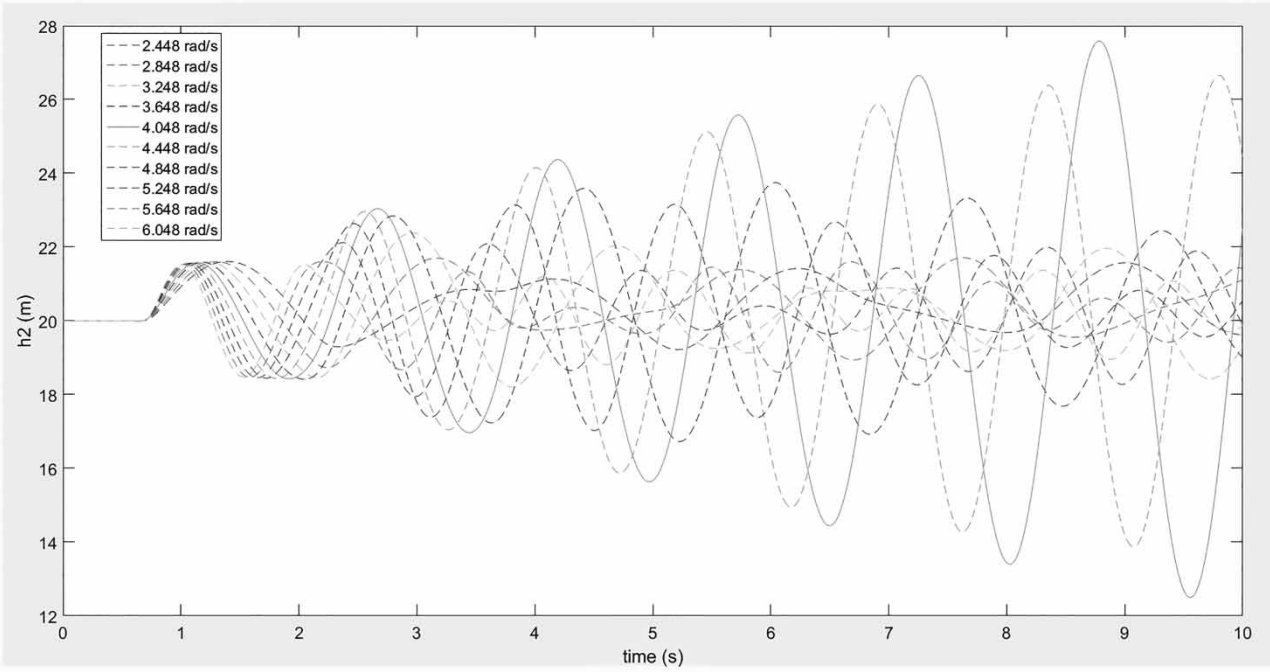

Figure 14 | Plots of h_2 of scenario B for different frequencies of q_1.

where B_{sl}*L corresponds to the integrator section in p_{21} and p_{22}; L/a corresponds to the delay section in p_{21}.

At high-frequency domain where $Freq > 1$ rad/s, the magnification line of p_{21} and p_{22} shows obvious oscillations. Previous research has proven that the

high-frequency variations of pressure head are caused by reflection of acoustic wave (Skulovich *et al.* 2015; Mitosek & Szymkiewicz 2016). In this paper, the authors use the water hammer equation to descrbe the high-frequency variations. Whereas a positive q_1 increases h_2, a positive q_2 decreases h_2; the high-frequency variations can be expressed as:

$$h_{2high}(t) = \frac{a}{A_f g} q_1(t-\tau) - \frac{a}{A_f g} q_2(t) \tag{25}$$

The linear model is obtained by adding up Equations (24) and (25). For scenario A it is:

$$\begin{aligned} &\frac{d}{dt}h(t) = \frac{1}{0.3090}[q_1(t-0.509) - q_2(t)], \\ &h_2(t) = h(t) + 1.65q_1(t-0.509) - 1.65q_2(t) \end{aligned} \tag{26}$$

For scenario B it is:

$$\begin{aligned} &\frac{d}{dt}h(t) = \frac{1}{0.00096}[q_1(t-0.780) - q_2(t)], \\ &h_2(t) = h(t) + 816q_1(t-0.780) - 816q_2(t) \end{aligned} \tag{27}$$

Although Equations (26) and (27) are similar to the IDZ model in form, the meaning of the parameters involved are completely different. In the IDZ model, the low-frequency variations of water depth are caused by water volume variations in the backwater area, and the high-frequency variations are caused by wave peaks. In the linear model for inverted siphon, the low-frequency variations are caused by wall deformation and the high-frequency variations are caused by reflection of acoustic wave.

Comparison of linear model with p_{21} and p_{22}

Figures 15–18 are comparisons of p_{21} and p_{22} with the linear model in frequency domain. Results show that the linear model is accurate in the low-frequency domain but less accurate in the high-frequency domain since it cannot present the oscillations. However, pressure head variations of very high frequencies dampen very quickly and rarely appear. Thus they are less important in the effectiveness of the linear model for practical use.

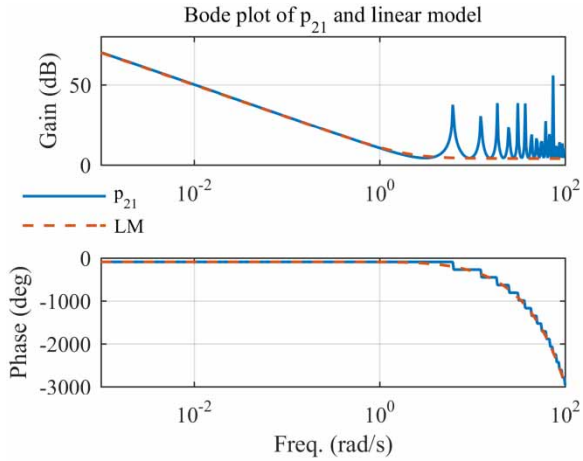

Figure 15 | Comparison of p_{21} with linear model of scenario A.

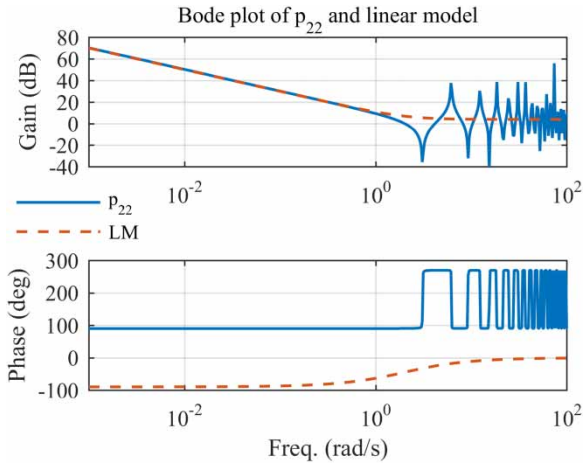

Figure 16 | Comparison of p_{22} with linear model of scenario A.

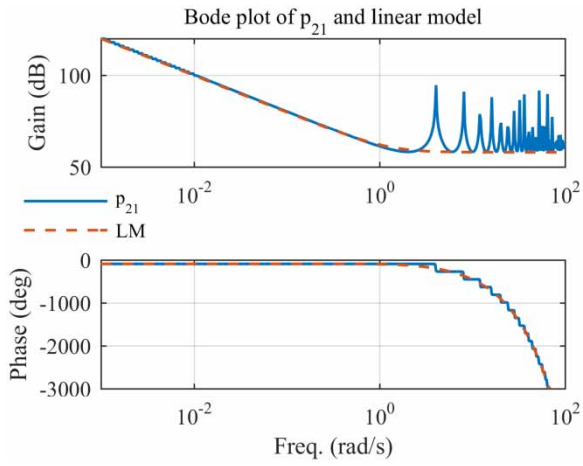

Figure 17 | Comparison of p_{21} with linear model of scenario B.

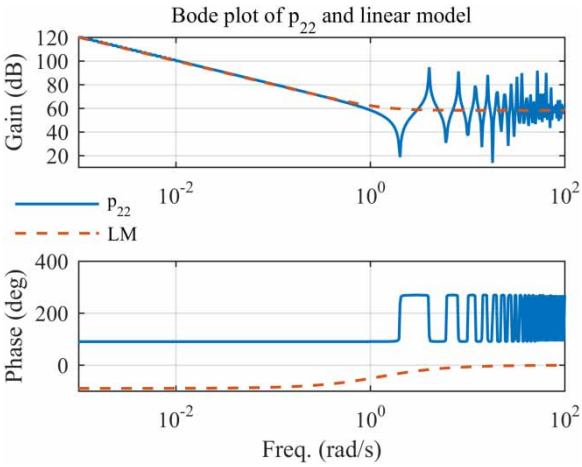

Figure 18 | Comparison of p_{22} with linear model of scenario B.

Comparison of linear model with simulation and experimental results

To verify the accuracy of the linear model in the time domain, the authors compare it with simulation results using the finite volume method. In numerical simulations, the S-V equations need to be expressed in a conservation form (Leon *et al.* 2008):

$$\frac{\partial \mathbf{U}}{\partial t} + \frac{\partial \mathbf{F}}{\partial x} = \mathbf{S} \tag{28}$$

where the flow variable vectors **U**, the flux vectors **F**, and the source term vectors **S** are:

$$U = \begin{bmatrix} \rho A \\ \rho v A \end{bmatrix}, F = \begin{bmatrix} \rho v A \\ \frac{(\rho v A)^2}{\rho A} + Ap \end{bmatrix}, S = \begin{bmatrix} 0 \\ (S_0 - S_f)\rho g A \end{bmatrix} \tag{29}$$

where p is the pressure that acts on the center of the cross-section. In this paper, a quasi-steady friction model is adopted (Ghidaoui Mohamed *et al.* 2002). A first-order Godunov-type scheme with a Roe solver is used for numerical simulation. The boundary condition employs the ghost cells proposed by Toro (2002).

In scenario A, the initial flow rate is 115 m^3/s, and a water tank is placed at the upstream end to provide a constant water head of 21.4 m. The ghost cell at the upstream boundary applies a constant pressure head of 21.4 m while the discharge adopts a transmissive condition. The ghost cell at the downstream boundary applies a constant discharge of 120 m^3/s while the pressure head adopts a transmissive condition. The distance step of simulation is 25.8 m, and the time step is 0.0242 s. The linear model of scenario A is written in incremental form as:

$$\Delta h_2(t) = \frac{\Delta t}{0.3090}\left[q_1\left(t - round\left(\frac{0.509}{\Delta t}\right)\right) - q_2(t)\right] + 1.65\Delta q_1\left(t - round\left(\frac{0.509}{\Delta t}\right)\right) - 1.65\Delta q_2(t) \tag{30}$$

where Δt is the time step. Figure 19 shows the pressure at the downstream end (P_{bv}) in the simulation results (*FVM*) and linear model (*Res*). The values of q_1 and q_2 used in Equation (30) are obtained from simulation results of finite volume method.

An experiment was carried out on scenario B; for details of the experiment refer to Bergant *et al.* (2011). In the experiment, a water tank is placed at the inlet to provide a constant water head of 21.4 m, the initial flow rate is 0.007 m^3/s, and a ball valve is set at the outlet to control the outflow rate. At the beginning of the experiment, the ball valve is closed immediately. In simulation, the distance step is 13.5 m, the time step is 0.0369 s, and the Courant number is 0.95. The ghost cell at the upstream boundary applies a constant pressure head of 21.4 m while the discharge adopts a transmissive condition. The ghost cell at

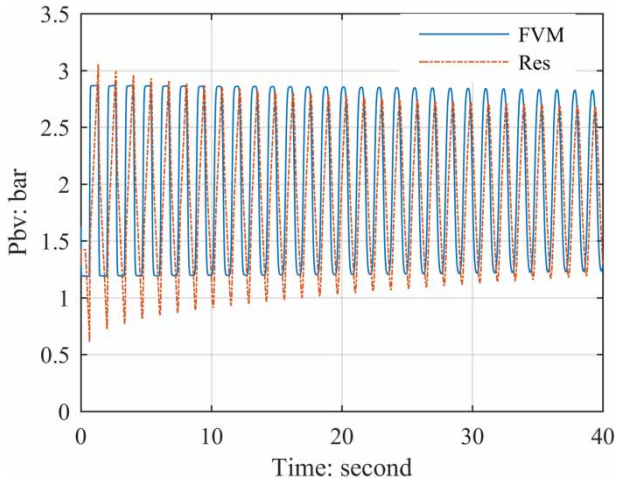

Figure 19 | Pressure at downstream end of simulation and linear model.

the downstream boundary applies a constant discharge of 0 m^3/s while the pressure head adopts a transmissive condition. The linear model of scenario B can be written in incremental form as:

$$\Delta h_2(t) = \frac{\Delta t}{0.00096}\left[q_1\left(t - round\left(\frac{0.780}{\Delta t}\right)\right) - q_2(t)\right] + 816\Delta q_1\left(t - round\left(\frac{0.780}{\Delta t}\right)\right) - 816\Delta q_2(t) \quad (31)$$

Figure 20 shows the pressure at ball valve (P_{bv}), *FVM* represents P_{bv} obtained using finite volume method, *Exp* represents P_{bv} obtained by experiments, *Res* represents P_{bv} obtained by Equation (31). The values of q_1 and q_2 used in Equation (31) are obtained from simulation results of finite volume method.

According to *Exp*, when the valve is closed a wave is generated at the ball valve. The P_{bv} changes in a periodical manner due to the reflection of acoustic wave between the inlet and the valve. At the first 5 seconds, some variations which are of higher frequency than wave reflection exist in the experimental data and then quickly disappear. From $t = 5$ s to $t = 20$ s, two or three frequencies of variations are present in P_{bv} while from $t = 20$ s to 40 s only one frequency of variations remains. In this process, the amplitude of pressure gradually decreases due to the stress-strain behavior.

As shown in Equations (24) and (25), the parameters in the linear model are determined by L, A_f, and a. Among them, only a is an implicit value which needs to be calibrated by experiments. In order to evaluate the influence of wave speed on the accuracy of the linear model, different values of wave speed are adopted in Equations (24) and (25). Herein, the L_2 norm is defined as an indicator of accuracy in comparison with FVM:

$$L_2 = \sqrt{\sum_{i=1}^{Nt} |p_{Res,i} - p_{FVM,i}|^2 \Delta t} \quad (32)$$

where p_{Res} is pressure computed using the linear model, p_{FVM} is pressure in simulation results of finite volume method, and Δt is the time step. The L_2 norms of different wave speed are shown in Figures 21 and 22.

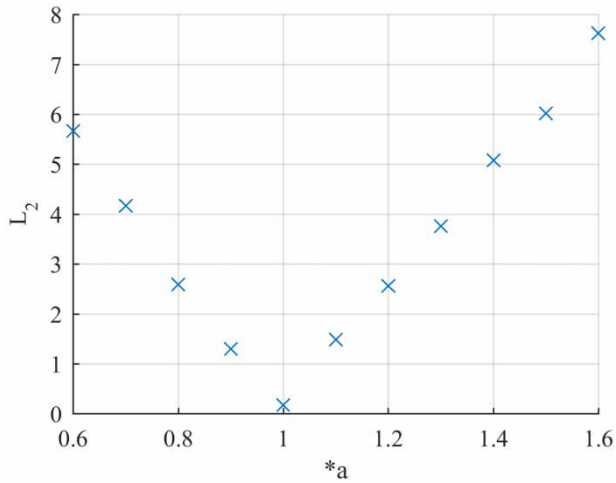

Figure 21 | L_2 norms of different wave speeds in scenario A.

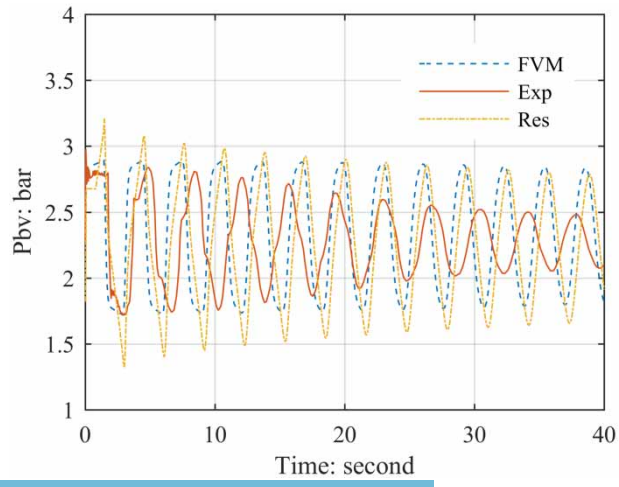

Figure 20 | P_{bv} of experimental data, simulation, and linear model.

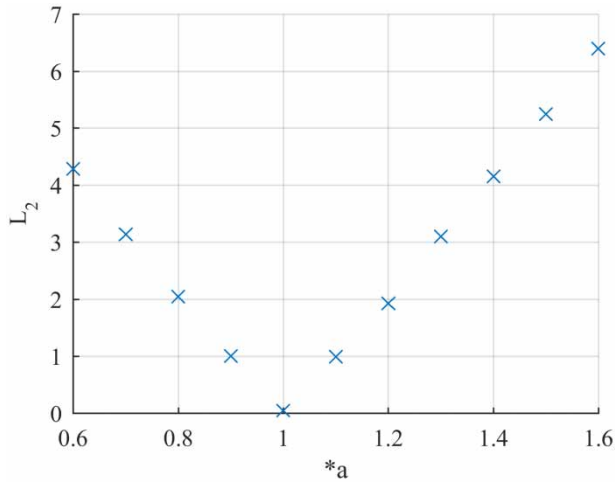

Figure 22 | L_2 norms of different wave speeds in scenario B.

The abscissa is the wave speed in multiples of the correct wave speed a. It can be seen that the minimum L_2 norm is achieved when a is used; the minimum L_2 norms are 0.177 and 0.044 for scenario A and B, respectively. The linear model is sensitive to the wave speed, when a false speed is used, the L_2 norm can reach to 6 and 7 for scenario A and B, respectively. Thus, a correct value of a is critical in the accuracy of the linear model. The value of a may be affected by the upstream structures in practice (Mitosek & Szymkiewicz 2016), so it needs to be calibrated by experiments.

INFLUENCE ON WATER FLUCTUATION OF INVERTED SIPHON

Finally, the linear model is applied to the model inverted siphon in a conceptualized water distribution system, shown as Figure 23. It consists of two open-channels and one inverted siphon. Open-channels 1 and 2 are prismatic with a trapezoidal cross-section while the inverted siphon has a circular cross-section. The wave speed in the inverted siphon is set at 1,014 m/s, and the slot width is 2.9943×10^{-5} m according to Equation (1). A gate is placed at the upstream end of open-channel 1 to control the inflow rate of the entire system. A weir is placed at the downstream end of open-channel 2. Model parameters are listed in Table 4. This model is simulated using the finite-difference method with a time step of 0.2 s and a distance step of 10 m for two open-channels and the inverted siphon.

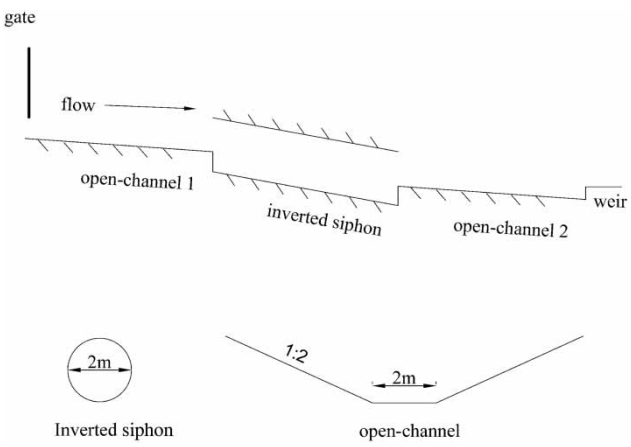

Figure 23 | Longitudinal sketches and cross-section of water distribution system.

Table 4 | Parameters of open-channel and inverted siphon

	Length (m)	Slope	Manning coefficient
Open-channel 1	1,000	5/10,000	0.015
Open-channel 2	1,000	5/10,000	0.015
Inverted siphon	2,000	1/2,000	0.014

The initial flow rate is 3 m^3/s, then at $t = 5$ min, the flow rate at the gate increases to 8 m^3/s and remains constant. Figure 24 shows that, at $t = 9$ min, h_1 and h_2 of the inverted siphon start to change. The variations of h_1 show obvious oscillations while the variations of h_2 are smaller and mild. This finding indicates that the inverted siphon can filter the high-frequency variations and decrease the amplitude of variations.

According to the linear model, variations of h_2 consist of low- and high-frequency parts. At the low-frequency domain, the deformation of siphon wall at the two ends are similar, the difference between h_1 and h_2 is frictional head loss h_f. Because of the transmissive condition in the inverted siphon, only the wave that moves from the upstream end to the downstream end is present. Thus, the high-frequency variations of h_2 can be computed using the first term at the right side of Equation (25):

$$h_{2high}(t) = \frac{a}{A_f g} q_1(t - \tau) \tag{33}$$

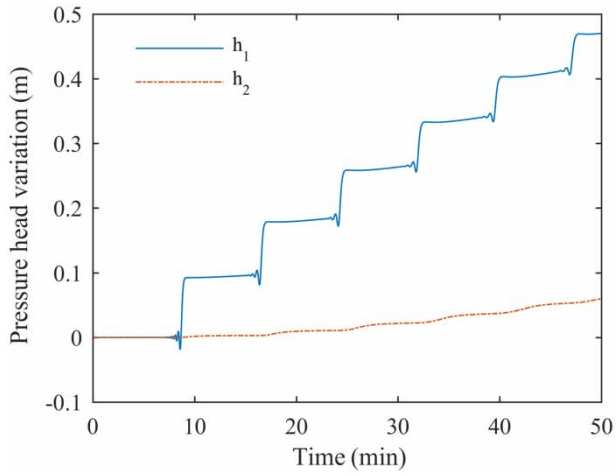

Figure 24 | Variations of h_1 and h_2 of inverted siphon.

The variations of h_1 can be determined similar to the second term at the right side of Equation (25):

$$h_{1high}(t) = \frac{a}{A_f g} q_1(t) \tag{34}$$

Combing the low-frequency and high-frequency variations, the expression of h_1–h_2 is:

$$h_1(t) - h_2(t) = h_f(t) + \frac{a}{A_f g} q_1(t) - \frac{a}{A_f g} q_1(t-\tau) \tag{35}$$

Because the time τ is very short, the following transformation can be made:

$$h_1(t) - h_2(t) = h_f(t) + \frac{a}{A_f g} \tau \left(\frac{d}{dt} q_1(t) \right) \tag{36}$$

where τ can be approximated by L/a. Then, Equation (36) becomes:

$$h_1(t) - h_2(t) = h_f(t) + \frac{L}{A_f g} \left(\frac{d}{dt} q_1(t) \right) \tag{37}$$

In this paper, the second term at the right side of Equation (37) is noted as h_i. The frictional head loss h_f is computed using the flow rate at the upstream end of the inverted siphon under the assumption of a quasi-steady flow condition. The comparisons between h_1–h_f, h_1–h_f–h_i and h_2 are shown in Figure 25. The L_2 norm between h_1–h_f and h_2 is 1.206 while the L_2 norm between h_1–h_f–h_i and h_2 is 0.026. This result shows that an inverted siphon reduces the fluctuation of water level in open canals. The effect can be quantified using Equation (37).

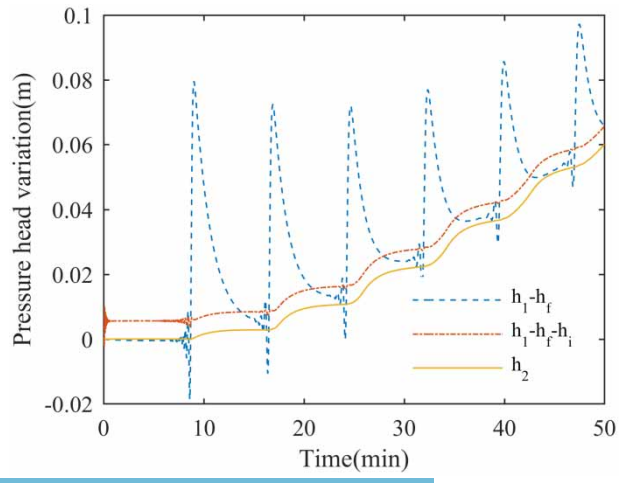

Figure 25 | Comparison of h_1–h_f, h_1–h_f–h_i with h_2.

CONCLUSIONS

A linear model relating the pressure head variations at the downstream end to the flow rate variations at two ends of an inverted siphon or pipe is proposed in this paper. The linear model divides the pressure head variations into low-frequency part and high-frequency part, which are caused by wall deformation and wave reflection, respectively. In the high-frequency domain, specific frequencies of flow rate variations at the two ends may cause a larger amplitude in pressure head variations as a resonance. An equation is proposed to compute these frequencies, i.e., Equation (20). For the low-frequency variations, the Preissmann slot method is adopted to derive a simplified relation between wall deformation and pressure head variations. While for the high-frequency variations, the water hammer equation is adopted to evaluate the pressure head variations caused by acoustic wave reflection. The parameters of the linear model are computed using L, a, and A_f. Two scenarios are studied in this paper, one is a large-scale inverted siphon and the other one is a PVC pipe. The accuracy of the linear model is verified in frequency domain using Bode plot in two scenarios. Then the pressure head computed using the linear model is compared with the simulation results of FVM in two scenarios. The accuracy of this model is based on an accurate speed of acoustic wave. The minimum L_2 norms are achieved when a correct wave speed is used. The minimum L_2 norms are 0.177 and 0.044 for the inverted siphon and the PVC pipe, respectively. When a false speed is used, the L_2 norms can reach 6 and 7 for the inverted siphon and the PVC pipe, respectively. Thus, a correct speed of acoustic wave is important to guarantee the accuracy of the linear model. The linear model is subsequently applied to describe an inverted siphon in a conceptualized water distribution system. Simulation results show that the inverted siphon can reduce water fluctuations. This effect is quantified by a frictional head loss h_f under the assumption of a quasi-steady flow and an inertia head

multipled by $L/(A_f g)$. On the basis of the aforementioned analysis, the following conclusions can be drawn:

1. An equation to compute the frequencies of flow rate variations at the two ends that may cause resonant pressure head variations in an inverted siphon or pipe is proposed. These frequencies are multiples of the wave reflection frequency between the two ends. In order to avoid damage of the siphon or pipe wall caused by pressure variations, flow rate variations around these frequencies should be avoided.
2. The pressure head variations in an inverted siphon or pipe can be divided into a low-frequency part and high-frequency part. The low-frequency part is caused by wall deformation while the high-frequency part is caused by the reflection of acoustic wave.
3. A linear model is proposed to calculate the pressure head variations at the downstream end of the inverted siphon using the flow rate variations at two ends. This model is applicable to other structures, such as pipes and tunnels, where pressurized flows are present. The low-frequency pressure head variations are related to the flow rate at two ends using a virtual slot width B_{sl}, which represents the ratio of wall deformation to pressure head variations. The high-frequency variations are computed using the water hammer equation. The linear model is sensitive to the speed of acoustic wave, but in practice, it needs to be calibrated by experiments to ensure the accuracy of the linear model.
4. An equation to quantify the reduction effect of an inverted siphon on the water fluctuations is proposed. The reduction effect can be computed using a frictional head loss under the assumption of a quasi-steady flow condition and an inertia head multiplied by $L/(A_f g)$.

The linear model proposed in this study can be used to build a coupled model of open-channel and pressured flows (i.e., syphon and tunnel), which can then optimize the feedback controller. These findings may be a reference for large water delivery systems.

ACKNOWLEDGEMENTS

The authors acknowledge the support of the NSFC grant 51979202.

SUPPLEMENTARY DATA

The Supplementary Data for this paper is available online at http://dx.doi.org/10.2166/hydro.2019.053.

REFERENCES

An, H., Lee, S., Noh, S. J., Kim, Y. & Noh, J. 2018 Hybrid numerical scheme of Preissmann slot model for transient mixed flows. *Water* **10** (7), 899.

Bergant, A., Hou, Q., Keramat, A. & Tijsseling, A. S. 2011 Experimental and numerical analysis of water hammer in a large-scale PVC pipeline apparatus. In: *Paper Presented at the 4th International Meeting on Cavitation and Dynamic Problems in Hydraulic Machinery and Systems*. University of Belgrade, Belgrade, Serbia.

Bertaglia, G., Ioriatti, M., Valiani, A., Dumbser, M. & Caleffi, V. 2018 Numerical methods for hydraulic transients in visco-elastic pipes. *Journal of Fluids and Structures* **81**, 230–254. doi: 10.1016/j.jfluidstructs.2018.05.004.

Brito, M., Sanches, P., Ferreira, R. M. L. & Covas, D. 2017 Experimental study of the transient flow in a coiled pipe using PIV. *Journal of Hydraulic Engineering* **143** (3), 04016087.

Clemmens, A. J. & Strand, R. J. 2010 Downstream-water-level control test results on the WM lateral canal. *Journal of Irrigation and Drainage Engineering* **136** (7), 460–469. doi:10.1061/(ASCE)IR.1943-4774.0000079.

Clemmens, A. J., Bautista, E., Wahlin, B. T. & Strand, R. J. 2005 Simulation of automatic canal control systems. *Journal of Irrigation and Drainage Engineering* **131** (4), 324–335. doi:10.1061/(ASCE)0733-9437(2005)131:4(324).

Clemmens, A., Tian, X., Overloop, P. & Litrico, X. 2015 Integrator delay zero model for design of upstream water-level controllers. *Journal of Irrigation and Drainage Engineering* **143**, B4015001. doi: 10.1061/(ASCE)IR.1943-4774.0000997.

Cunge, J., Holly, F. & Verwey, A. 1980 *Practical Aspects of Computational River Hydraulics*. Pitman, New York, USA.

Dazzi, S., Maranzoni, A. & Mignosa, P. 2016 Local time stepping applied to mixed flow modelling. *Journal of Hydraulic Research* **54** (2), 145–157. doi: 10.1080/00221686.2015.1132276.

Duan, H.-F., Lee, P. J., Ghidaoui, M. S. & Tung, Y.-K. 2011 Leak detection in complex series pipelines by using the system frequency response method. *Journal of Hydraulic Research* **49** (2), 213–221. doi: 10.1080/00221686.2011.553486.

Foo, M., Ooi, S. K. & Weyer, E. 2012 Modelling of rivers for control design. In: *System Identification, Environmental Modelling, and Control System Design* (L. Wang & H. Garnier, eds). Springer, Londom, UK, pp. 423–447.

Foo, M., Ooi, S. K. & Weyer, E. 2014 System identification and control of the broken river. *IEEE Transactions on Control Systems Technology* **22** (2), 618–634.

Ghidaoui Mohamed, S., Mansour Sameh, G. S. & Zhao, M. 2002 Applicability of quasisteady and axisymmetric turbulence models in water hammer. *Journal of Hydraulic Engineering* **128** (10), 917–924. doi: 10.1061/(ASCE)0733-9429(2002)128:10(917).

Guan, G., Clemmens, A. J., Kacerek, T. F. & Wahlin, B. T. 2011 Applying water-level difference control to Central Arizona Project. *Journal of Irrigation and Drainage Engineering-ASCE* **137** (12), 747–753. doi: 10.1061/(ASCE)IR.1943-4774.0000351.

Leon, A. S., Ghidaoui, M. S., Schmidt, A. R. & Garcia, M. H. 2008 Efficient second-order accurate shock-capturing scheme for modeling one- and two-phase water hammer flows. *Journal of Hydraulic Engineering* **134** (7), 970–983.

Li, L., Zhu, D. Z. & Huang, B. 2018 Analysis of pressure transient following rapid filling of a vented horizontal pipe. *Water* **10** (11), 1698.

Lin, J., Wang, X. & Ghidaoui Mohamed, S. 2019 Theoretical investigation of leak's impact on normal modes of a water-filled pipe: small to large leak impedance. *Journal of Hydraulic Engineering* **145** (6), 04019017. doi: 10.1061/(ASCE)HY.1943-7900.0001606.

Litrico, X. & Fromion, V. 2004 Frequency modeling of open-channel flow. *Journal of Hydraulic Engineering* **130** (8), 806–815. doi:10.1061/(ASCE)0733-9429(2004)130:8(806).

Malaterre, P.-O., Rogers, D. C. & Schuurmans, J. 1998 Classification of canal control algorithms. *Journal of Irrigation and Drainage Engineering* **124** (1), 3–10. doi:10.1061/(ASCE)0733-9437(1998)124:1(3).

Maranzoni, A. & Mignosa, P. 2018 Numerical treatment of a discontinuous top surface in 2D shallow water mixed flow modeling. *International Journal for Numerical Methods in Fluids* **86** (4), 290–311. doi: 10.1002/fld.4418.

Mitosek, M. & Szymkiewicz, R. 2016 Reservoir influence on pressure wave propagation in steel pipes. *Journal of Hydraulic Engineering* **142** (8), 06016007.

Okhravi, S., Eslamian, S. & Fathianpour, N. 2017 Assessing the effects of flow distribution on the internal hydraulic behavior of a constructed horizontal subsurface flow wetland using a numerical model and a tracer study. *Ecohydrology & Hydrobiology* **17** (4), 264–273. https://doi.org/10.1016/j.ecohyd.2017.07.002.

Overloop, P. J. v., Schuurmans, J., Brouwer, R. & Burt, C. M. 2005 Multiple-model optimization of proportional integral controllers on canals. *Journal of Irrigation and Drainage Engineering* **131** (2), 190–196. doi:10.1061/(ASCE)0733-9437(2005)131:2(190).

Rogers, D. C., Kacerek, T. F. & Gooch, R. S. 1993 Field data for verifying canal unsteady flow models. *Journal of Irrigation and Drainage Engineering* **119** (4), 679–692. doi:10.1061/(ASCE)0733-9437(1993)119:4(679).

Sadeghi, S. H., Mousavi, S. F., Eslamian, S. S., Ansari, S. & Alemi, F. 2012 A unified approach for computing pressure distribution in multi-outlet irrigation pipelines. *Iranian Journal of Science and Technology-Transactions of Civil Engineering* **36** (C2), 209–223.

Schuurmans, J., Bosgra, O. H. & Brouwer, R. 1995 Open-channel flow model approximation for controller design. *Applied Mathematical Modelling* **19** (9), 525–530. http://dx.doi.org/10.1016/0307-904X(95)00053-M.

Schuurmans, J., Clemmens, A. J., Dijkstra, S., Hof, A. & Brouwer, R. 1999 Modeling of irrigation and drainage canals for controller design. *Journal of Irrigation and Drainage Engineering* **125** (6), 338–344. doi:10.1061/(ASCE)0733-9437(1999)125:6(338).

Shahdany, S. M. H., Majd, E. A., Firoozfar, A. & Maestre, J. M. 2016 Improving operation of a main irrigation canal suffering from inflow fluctuation within a centralized model predictive control system: case study of Roodasht Canal, Iran. *Journal of Irrigation and Drainage Engineering*. **142** (11). doi: 10.1061/(ASCE)IR.1943-4774.0001087.

Skulovich, O., Sela Perelman, L. & Ostfeld, A. 2015 Optimal closure of system actuators for transient control: an analytical approach. *Journal of Hydroinformatics* **18** (3), 393–408. doi: 10.2166/hydro.2015.121.

Toro, E. 2002 *Shock Capturing Methods for Free Surface Shallow Water Flows*. John Wiley and Sons, Chichester, UK.

Wahlin, B. & Zimbelman, D. 2018 Canal automation for irrigation systems: American society of civil engineers manual of practice number 131. *Irrigation and Drainage* **67** (1), 22–28. doi: 10.1002/ird.2140.

Wang, X. & Ghidaoui, M. S. 2018 Identification of multiple leaks in pipeline: linearized model, maximum likelihood, and super-resolution localization. *Mechanical Systems and Signal Processing* **107**, 529–548. https://doi.org/10.1016/j.ymssp.2018.01.042.

Zhu, Y., Duan, H. F., Li, F., Wu, C. G., Yuan, Y. X. & Shi, Z. F. 2018 Experimental and numerical study on transient air–water mixing flows in viscoelastic pipes. *Journal of Hydraulic Research* **56** (6), 877–887. doi: 10.1080/00221686.2018.1424045.

First received 7 March 2019; accepted in revised form 29 August 2019. Available online 14 October 2019